INSTITUTE OF PHYSICS PUBLISHING MEASUREMENT SCIENCE AND TECHNOLOGY

Meas. Sci. Technol. **15** (2004) 2029–2038 PII: S0957-0233(04)76107-X

A method for three-dimensional particle sizing in two-phase flows

Francisco Pereira[1] **and Morteza Gharib**

Graduate Aeronautical Laboratories, California Institute of Technology, Pasadena, CA 91125, USA

E-mail: f.pereira@insean.it and mory@caltech.edu

Received 9 February 2004, in final form 21 June 2004
Published 26 August 2004
Online at stacks.iop.org/MST/15/2029
doi:10.1088/0957-0233/15/10/012

Abstract

A method is devised for true three-dimensional (3D) particle sizing in two-phase systems. Based on a ray-optics approximation of the Mie scattering theory for spherical particles, and under given assumptions, the principle is applicable to intensity data from scatterers within arbitrary interrogation volumes. It requires knowledge of the particle 3D location and intensity, and of the spatial distribution of the incident light intensity throughout the measurement volume. The new methodology is particularly suited for Lagrangian measurements: we demonstrate its use with the defocusing digital particle image velocimetry technique, a 3D measurement technique that provides the location, intensity and velocity of particles in large volume domains. We provide a method to characterize the volumetric distribution of the incident illumination and we assess experimentally the size measurement uncertainty.

Keywords: two-phase flows, defocusing digital particle image velocimetry, particle sizing

1. Introduction

The size distribution and the number density of particles or bubbles, and the resulting void fraction, are essential elements for the investigation of multi-phase phenomena such as the combustion processes, the transport and dispersion of solid particles, the coalescence and break-up of gas particles in bubbly flows or of liquid droplets in sprays. These quantities are also key parameters in assessing and modelling the collective particle interaction with the flow dynamics.

Size measurements have been reported in a variety of industrial applications and in many disciplines of fundamental and applied engineering sciences, ranging from chemistry to medicine to combustion. The techniques available can be roughly classified into two broad categories: (i) the single particle measurement techniques, characterized by small sample volumes and restricted to measuring a single particle at a time; (ii) the ensemble techniques, characterized by line-of-sight sample volumes and providing the average size distribution of a group of particles.

In the field of fluid research, Billet (1985) and O'Hern and Gore (1991) provide reviews of the methods available, briefly itemized hereafter. Acoustical approaches are based either on the attenuation of sound by particles or on their acoustical backscatter, and have been primarily used to investigate the dense bubble clouds in the wakes of ocean vessels, a source of acoustical and optical signature (Medwin 1977, Vagle and Farmer 1992). O'Hern *et al* (1988) and Sheng and Irons (1991) used electrical or impedance probes to measure void fractions of cavitation nuclei in the ocean. In the discipline of chemical engineering, Zhu *et al* (1993) have reported density measurements of air bubbles.

Single particle techniques are mostly of optical nature: broadband or white light scattering (Katz *et al* 1983, Hofeldt and Hanson 1991), photographic methods (Hawighorst 1983), holography (Thompson 1974, d'Agostino and Green 1992), phase-Doppler detection by light scattering interferometry (Brena de la Rosa *et al* 1989, Bachalo 1994), video imaging (Tassin and Nikitopoulos 1995), particle defocus (Bongiovanni *et al* 1997) and gamma or neutron radiography (Mishima and Hibiki 1998). The reader will find a useful source of bibliographical references

[1] Present address: INSEAN, Rome, Italy.

on laser-based techniques in the review compiled by Black *et al* (1996).

The light scattering techniques are among the simplest to implement, the principle being that the measured scattered intensity of a particle can be uniquely related to its size. The Lorenz–Mie theory is the underlying basis for this principle, as it shows that large spherical particles, roughly greater than 10–20 μm, scatter light in proportion to the square of the diameter. As the particles become smaller, and in particular for submicron particles, we enter the Rayleigh scattering range, where different laws apply. The mathematical formulation of the Lorenz–Mie theory is extensively discussed in reference texts such as those by Van de Hulst (1957) and Bohren and Huffman (1983).

Another important issue in the particle sizing problem is the ability of a given technique to provide the size information in large interrogation domains. It is noticeable that the techniques cited above are either global and integral, or single point and restricted to small control volumes. None of them can claim to be multidimensional in the strict sense, except the holography-based methods. The term has only recently been used in the field of particle sizing for two relatively new techniques. The first is the generically called interferometric particle imaging (IPI), which is based on the interference between the reflection and the first-order refractive scattering patterns of spherical particles. It was first introduced by König *et al* (1986), then improved by Glover *et al* (1995) and more recently by Maeda *et al* (2000), who extended the principle to the measurement in a plane. The second technique is known as global phase Doppler (GPD) and employs two parallel laser light sheets at an angle to account for higher refractive scattering orders, see Damaschke *et al* (2001). Yet, the ability of these techniques to map the third spatial dimension is expected to be modest in terms of accuracy and limited to small depth ranges, as they employ the out-of-focus image size to retrieve the depth information. It is known that 'depth-from-out-of-focus' techniques display a poor level of performance both in spatial accuracy (Subbarao and Surya 1994) and in sizing when it comes to using the blur information as a size indicator (Bongiovanni *et al* 1997). The two new techniques are also inherently restricted to low particle concentrations and narrow depth range because of the overlap and size of the blurred particle images (Damaschke *et al* 2002).

In the following sections, we use the light scattering approach to develop a novel methodology for the size measurement of mono-species particle systems in actual three-dimensional volumes. Given the optical properties of the particles and of the surrounding medium, the method is based on the light scattering properties of particles, described by a ray-optics approximation of the general Mie theory for large spheres, in combination with the three-dimensional spatial location of particles. We use here the defocusing digital particle image velocimetry (DDPIV) technique (Pereira *et al* 2000, Pereira and Gharib 2002) to validate the proposed approach.

2. Light scattering by a sphere

Let us consider a sphere of radius a and of absolute refractive index n_1, placed in a medium of absolute refractive index n_2. We define the relative refractive index $m = n_1/n_2$, the wavenumber $k = 2\pi/\lambda$, where λ is the wavelength of the incident light in the surrounding medium, and the parameter $x = ka$. x is the ratio of the sphere circumference to the wavelength. We also define the scattering angle θ, with 0° being the total forward scatter mode.

The Lorenz–Mie theory provides the rigorous, analytical solution to the problem of scattering of light by a single, homogeneous spherical particle of arbitrary size illuminated by a plane wave propagating through the surrounding medium (Van de Hulst 1957). This theory relates the particle/bubble scattered intensity to the sphere size, but is of rather difficult practical implementation. However, the scattering pattern can be fairly approximated using the geometrical optics light-scattering theory, except for some exceptional scattering angles and under the following two conditions:

- $x \gg 1$: the radius a of the sphere is much larger than the wavelength of the incident light. In practice, sphere radii larger than 5–10 μm should be considered.
- the phase shift $\rho = 2x(m-1)$ must be large enough, i.e. the refractive index of the particle must differ sufficiently from that of its surroundings.

Ungut *et al* (1981) report that, for light scattering in the near forward direction, the difference between the two theories is of the order of 10%, for particles larger than 10 μm and with less than 5% deviation from sphericity.

We base our approach on this ray-optics approximation. For our analytical derivation of the scattered intensity, we consider a sphere with a real refractive index m and radius a, such that $x \gg 1$. For simplicity of the derivation, we assume that $m > 1$ in a first step before extending the results for $m < 1$. Amplitude and phase of the scattered light may be expressed by means of the complex amplitude functions $S_1(\theta)$ and $S_2(\theta)$, which depend exclusively on the scattering angle θ. The index 1 refers to the incident light and scattered light with electric vibration perpendicular to the scattering plane (also referred to as perpendicular or s polarization). The index 2 refers to the electric vibration in this plane (also called parallel or p polarization). The flux of light intensity I (units are W m^{-2}) scattered at the angle θ is expressed by

$$I(\theta) = \frac{1}{2}[I_1(\theta) + I_2(\theta)] \qquad \text{with} \quad I_1(\theta) = \frac{i_1}{k^2 r^2} I_{0,1}$$
$$I_2(\theta) = \frac{i_2}{k^2 r^2} I_{0,2} \qquad i_1 = |S_1(\theta)|^2, \quad i_2 = |S_2(\theta)|^2 \tag{1}$$

where $I_{0,1}$ and $I_{0,2}$ are, respectively, the perpendicular and parallel plane-polarized parts of the incident wavefront intensity and r is the distance to the centre of the sphere at the scattering angle θ.

In the ray-optics approach, a light ray hitting the surface of a sphere is split into a reflected part and a refracted part, as illustrated in figure 1. The direction of the refracted ray follows from Snell's law, whereas the intensity and phase follow from the Fresnel coefficients. A similar operation occurs when the refracted ray hits the sphere surface in its internal travel: part of it is refracted and leaves the sphere whereas the other part is reflected internally for further and infinite repetition of the splitting process. We describe the contact surfaces by the parameter p, which is the order of the ray reflection/refraction. The rays from surface $p = 0$ are

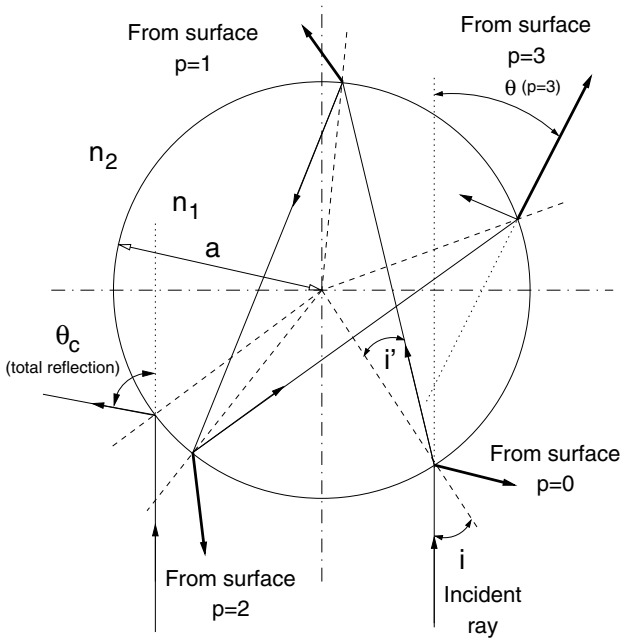

Figure 1. Light paths through a sphere with $n_1 > n_2$ and radius a.

essentially side and backscatter, whereas the rays from surface $p = 1$ are mostly forward scattering.

The Fresnel reflection coefficients are given by

$$r_1 = \frac{\cos i - m\cos i'}{\cos i + m\cos i'}, \qquad r_2 = \frac{m\cos i - \cos i'}{m\cos i + \cos i'} \tag{2}$$

where the angles i and i' represent the angles between the normal to the contact surface and the incident and the refracted beams, respectively, and are related by Snell's relation $\sin i' = \sin i/m$. The coefficients r_1 and r_2 are the ratio of the amplitude of the reflected wave to the amplitude of the incident wave, the index 1 being relative to the s polarization and the index 2 to the p polarization. The reflected fractions of the energy are r_1^2 and r_2^2 and, consequently, the refracted parts of the energy are $1 - r_1^2$ and $1 - r_2^2$. We denote these parts by ε_1^2 and ε_2^2. ε_1 is defined by

$$\begin{aligned} \varepsilon_1 &= r_1 && \text{for} \quad p = 0 \\ \varepsilon_1 &= \left(1 - r_1^2\right)(-r_1)^{p-1} && \text{for} \quad p > 0 \end{aligned} \tag{3}$$

and the same relations with index 2 hold for the other polarization.

The scattering angle θ represents the total deviation angle at surface p and is related to the incident and refracted angles i and i' at the entry surface ($p = 0$) by the relation

$$\theta = 2(pi' - i) - (p-1)\pi \qquad \text{with} \quad i' = \arcsin\frac{\sin i}{m}$$
$$\text{and} \quad p = 0, 1, 2, \ldots. \tag{4}$$

The incoming pencil of light, incident on surface $p = 0$, is characterized by $\mathrm{d}i$ and $\mathrm{d}\phi$ where ϕ is the azimuthal angle, i.e. the angle in a plane perpendicular to figure 1 and going through the sphere centre. The flux of intensity in this pencil is given by

$$I'_{0,1} = I_{0,1}a^2 \sin i \cos i \, \mathrm{d}i \, \mathrm{d}\phi \tag{5}$$

with the respective expression for $I'_{0,2}$.

Instead, the pencil of light emerging from surface p spreads into a solid angle $\sin\theta \, \mathrm{d}\theta \, \mathrm{d}\phi$, and the flux of light intensity at a distance r from the sphere is spread over an area r^2 times this solid angle. Additionally, only a portion ε_1^2 or ε_2^2 of the respective polarization is emerging. Therefore, the flux of light intensity going through this area is expressed by

$$I_1(\theta) = \frac{\varepsilon_1^2 I'_{0,1}}{r^2 \sin\theta \, \mathrm{d}\theta \, \mathrm{d}\phi} = \varepsilon_1^2 I_{0,1}\frac{a^2}{r^2}D$$
$$\text{with} \quad D = \frac{\sin i \cos i}{(\sin\theta)\,\mathrm{d}\theta/\mathrm{d}i} \quad \text{and} \quad \frac{\mathrm{d}\theta}{\mathrm{d}i} = 2\left(p\frac{\tan i'}{\tan i} - 1\right)$$
$$\text{from equation (4)} \tag{6}$$

with the corresponding formulae for $I_2(\theta)$. D is called the divergence.

Comparison with equation (1) yields the expressions for i_1 and i_2:

$$i_1(\theta) = x^2\varepsilon_1^2 D, \qquad i_2(\theta) = x^2\varepsilon_2^2 D \tag{7}$$

where $x = ka$.

If natural light of intensity I_0 is incident on the sphere, the scattered light in any direction has partial linear polarization. Therefore, the total scattered intensity at angle θ can be written as

$$\begin{aligned} I(\theta) &= \frac{i_1 + i_2}{2k^2r^2} I_0 \\ &= \frac{\varepsilon_1^2 + \varepsilon_2^2}{2}\frac{a^2}{r^2} I_0 D. \end{aligned} \tag{8}$$

Equation (8) is the ray-optics approximation of the Mie formulation for the scattered intensity by a large sphere.

The geometrical optics approximation fails when the outgoing beams have a point of inflection (the so-called rainbow beams) or when these beams are parallel to, but not coincident with, the axis. This latter situation occurs near the angles $\theta = 0^\circ$ and $\theta = 180^\circ$. Moreover, the diffraction scattering around the sphere, which gives rise to the Fraunhofer diffraction pattern, is not accounted for by the formulation.

For a relative refractive index $m' = 1/m$ (smaller than 1, as in the case of an air bubble in water), the extension of the theory is straightforward and is performed by interchanging in the previous relations i with i' and by replacing m by $1/m$. The relative energy distribution among various values of p is the same as it was for m, but the corresponding fractions of the incident light are scaled down by a factor m^2. Instead, the angular distribution of the scattered intensity (reflected and refracted) does not remain the same, for the scattering angle θ is different when i and i' are interchanged in equation (4); the only exception is for $p = 1$. In that case, the angular distribution is exactly the same for m and $1/m$ except for a scale factor m^2 in the intensities.

3. Working hypothesis

When integrating equation (8) over a range of angles θ and excluding the case of total reflection, the distribution of the scattered energy is largely predominant for the surface $p = 1$ for relative refractive indices m smaller or larger than 1 (Born and Wolf 1980). Davis (1955) and Dean and Marston (1991) use this approach to calculate the angular distribution of the light scattered by an air bubble in water. The latter work shows that nearly all the energy is scattered in the general forward direction from 0° to the critical scattering angle $\theta_c = 82.8°$, where the transition from partial to total reflection occurs (see figure 1).

In this work, the underlying hypothesis is that the scattered intensity of our particles is essentially from surface $p = 1$, i.e. forward scattering, and we will restrict our calculations to this surface in our further derivations. Total reflection ($p = 0$) and higher order scattering ($p > 1$) are therefore excluded.

4. Practical implementation

Equation (8) provides the radius a of a particle if the four following unknowns are resolved: the distance r to the particle, the scattering angle θ, the particle scattering intensity $I(\theta)$ and the incident wavefront I_0. r, θ and $I(\theta)$ can be determined using a three-dimensional measurement technique such as the DDPIV (Pereira and Gharib 2002), which provides the spatial coordinates of particles in a volumetric domain, and a measure of their scattered intensity. Other techniques are available to obtain the same information, in particular those based on photogrammetry and holography.

We propose hereafter a procedure to determine I_0. We rewrite equation (8) as a function of a, θ, m and of the particle three-dimensional location $\mathbf{P}$:

$$I(a,\theta,\mathbf{P})|_m = K(\theta,\mathbf{P})|_m I_0(\mathbf{P}) a^2$$
$$\text{with} \quad K(\theta,\mathbf{P})|_m = \left.\frac{\varepsilon_1^2+\varepsilon_2^2}{2}\frac{D}{r^2}\right|_m \quad \text{and} \quad r = \|\mathbf{P}\| \qquad (9)$$

where $\mathbf{P}$ is a vector defined by the triplet of coordinates (X, Y, Z). ε_1, ε_2 and D are defined by equations (3) and (6).

4.1. Calculation of r, θ and K

The distance r from the particle centre to the origin of the measurement system is given by the triplet of experimentally determined coordinates (X, Y, Z) of its location vector $\mathbf{P}$:

$$r = \|\mathbf{P}\| = \sqrt{X^2+Y^2+Z^2}. \qquad (10)$$

If θ_0 is the mean orientation angle of the illumination source with respect to the Z-axis, then we define the local scattering angle θ by

$$\theta = \theta_0 + \tan^{-1}\frac{\sqrt{X^2+Y^2}}{|Z|}. \qquad (11)$$

$K(\theta,\mathbf{P})|_m$ of equation (9) requires the calculation of the energy parts ε_1 and ε_2, and of the divergence term D. These terms are functions of the incident and refracted angles i and i' on the entry surface $p = 0$ (see figure 1), as per equations (2) and (3), and equation (6). The particle size a being roughly three to four orders of magnitude smaller than the scattering distance r, we assume that the incident and scattered light rays are passing through the particle centre defined by $\mathbf{P}(X, Y, Z)$. Using equation (4) and for $p = 1$, which is our working condition, we show that i and i' are related to θ by

$$i = -\sin^{-1}\frac{A}{\sqrt{A^2+B^2}} \qquad i' = \sin^{-1}\frac{\sin i}{m} \quad \text{(Snell's law)}$$
$$\text{with} \quad A = \sin\frac{\theta}{2} \quad \text{and} \quad B = \cos\frac{\theta}{2} - \frac{1}{m} \qquad (12)$$

where $m = n_1/n_2$ is the relative refractive index.

4.2. Incident wavefront intensity

In practical situations, the real distribution of the incident light intensity $I_0(\mathbf{P})$ is not know *a priori* and is likely to be non-planar, unlike the ideal situation used in the above derivations. $I_0(\mathbf{P})$ characterizes the non-uniformity of the light source used in an experiment, the fluctuations in time of the light intensity, and integrates the intensity variations introduced by the experimental setup. In an effort to accommodate this problem, Billet (1986) used a probabilistic correction procedure: based on a matrix inversion scheme, the method accounts for the non-uniformity of the intensity across the laser beam in a light-scattering system designed to measure the size of cavitation nuclei. Katz *et al* (1983) used a broadband light-scattering system, and applied a similar correction procedure. In both cases, the system needed to be calibrated, through a Monte Carlo simulation or by measuring the size of electrolytically produced bubbles rising at terminal velocity across the sample volume.

The spatial matrix $I_0(\mathbf{P})$ of the incident wavefront intensity can be experimentally determined using calibrated solid microspheres with radius a_0 and a relative refractive index $m_0 > 1$ (for instance, $m_0 \approx 1.128$ for glass in water). This procedure has three main advantages:

(i) solid monosize calibrated particles are used, hence avoiding the difficult task of generating monosize bubbles or drops;
(ii) natural or non-polarized light can be used;
(iii) the non-uniformity of the illumination is accounted for.

From equation (9), $I_0(\mathbf{P})$ is thus expressed by

$$I_0(\mathbf{P}) = \frac{I(a_0,\theta,\mathbf{P})|_{m_0}}{K(\theta,\mathbf{P})|_{m_0} a_0^2} \qquad (13)$$

where $I(a_0,\theta,\mathbf{P})|_{m_0}$ is the experimental volumetric dataset of the calibrated scatterers intensity.

4.3. Particle size

Let consider a sphere with radius a and relative refractive index m_1.

If $m_1 > 1$ ($m_1 \approx 4/3$ for a water droplet in air), then the radius a of the sphere can be directly calculated with equation (9) from the measurement of the scattered intensity $I(a,\theta,\mathbf{P})|_{m_1}$ and from the spatial distribution of $I_0(\mathbf{P})$ determined using equation (13):

$$a = \left[\frac{I(a,\theta,\mathbf{P})|_{m_1}}{K(\theta,\mathbf{P})|_{m_1} I_0(\mathbf{P})}\right]^{\frac{1}{2}} \qquad \text{with} \quad m_1 > 1. \qquad (14)$$

The definition of $K(\theta,\mathbf{P})|_{m_1}$ is given in equation (9).

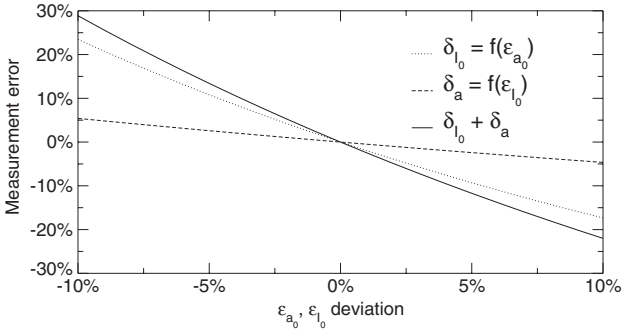

Figure 2. Theoretical errors from calibration (δ_{I_0}) and intensity variations (δ_a).

If $m_1 < 1$ ($m_1 \approx 3/4$ for an air bubble in water), the scattered intensity is related to that of a sphere with an inverse relative refractive index $m_2 = 1/m_1$ by

$$I(a, \theta', \mathbf{P})|_{m_1} = \frac{1}{m_2^2} I(a, \theta, \mathbf{P})|_{m_2} \tag{15}$$

θ' follows from the fact that the scattering angle is different for m_1 and for its inverse m_2, according to equation (4). However, we assessed earlier that the surface $p = 1$ is the predominant scattering surface in the absence of total reflection. Hence, if we consider this surface only, θ and θ' are identical.

Consequently, the radius a of a sphere in the ray-optics approximation and for $m_1 < 1$ is given by

$$a = m_2 \left[\frac{I(a, \theta, \mathbf{P})|_{m_1}}{K(\theta, \mathbf{P})|_{m_2} I_0(\mathbf{P})} \right]^{\frac{1}{2}} \qquad \text{with} \quad m_1 < 1$$
$$\text{and} \quad m_2 = \frac{1}{m_1} \tag{16}$$

with $K(\theta, \mathbf{P})|_{m_2}$ defined by equation (9).

5. Errors

From a theoretical standpoint, i.e. assuming a perfect, error-free measurement instrument and strictly working in the context of the ray-optics approach proposed here, there exist two types of errors that may affect the measurement. The first derives from the fact that the calibrated particles used for the calibration of the incident intensity using equation (13) are usually not exactly mono-dispersed. The second source of error regards the spatial and/or temporal fluctuations of the incident intensity distribution during the measurements, either because the intensity flux is variable in time or because the source setup differs from the calibration setup.

If ε_{a_0} is the deviation of the calibration radius a_0 and ε_{I_0} is the deviation of the intensity flux, then we can define the measurement errors

$$\delta_{I_0} = \left(1 + \varepsilon_{a_0}\right)^{-2} - 1, \qquad \delta_a = \left(1 + \varepsilon_{I_0}\right)^{-\frac{1}{2}} - 1 \tag{17}$$

respectively the measurement errors on I_0 and on the particle size a using equation (14) or equation (16).

Figure 2 represents δ_{I_0} and δ_a and the sum of both, which is the total deviation. The errors that derive from calibration are found to be preponderant with respect to the errors that derive from the light intensity fluctuations. Thus, particular care should be taken in selecting the calibration particles.

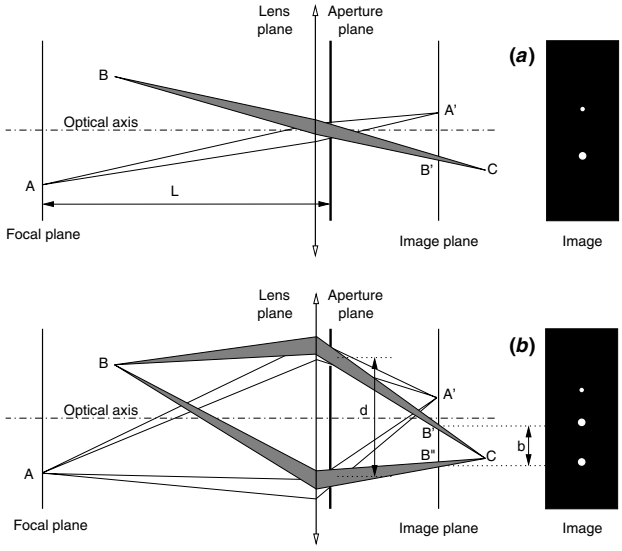

Figure 3. (*a*) Standard imaging system and (*b*) the defocusing concept.

Regarding the light source, the intensity flux should be steady in time for a continuous source, or should have acceptable repeatability if one uses a flash/pulsed illumination system. In all situations, the calibration and the measurement setups should be exactly, or very closely, the same.

6. Experimental assessment

In the following study, we intend to validate the proposed methodology using the prototype DDPIV instrument developed by Pereira *et al* (2000). This instrument has been designed for the instantaneous mapping of the three-dimensional coordinates and scattered intensity of particles in a $300 \times 300 \times 300\,\text{mm}^3$ volume.

6.1. Basics of the defocusing DPIV (DDPIV) technique

In a typical 2D imaging system consisting of a converging lens and of an aperture, as represented in figure 3(*a*), a point A located on the object plane (or reference plane) appears focused as A′ on the image plane (or sensor plane). A point B located between the reference plane and the lens system is projected as a blurred image B′.

The DDPIV technique uses a mask with two or more apertures shifted away from the optical axis to obtain multiple images from each scattering source. In figure 3(*b*), a two-aperture system produces a pair of images B′ and B″ of the same source object point B. The image shift b between those two images, which is caused by the off-axis apertures, is related to the depth location of the source point.

Upon measurement of the image coordinates (x', y') and (x'', y'') of B′ and B″, hence of the image shift b, the space coordinates (X, Y, Z) of B are given by

$$\begin{cases} X = F_x(x', x'', Z) \\ Y = F_y(y', y'', Z) \\ Z = F_z(d, L, M, b) \end{cases} \tag{18}$$

where d and L are geometrical characteristics of the optical system, respectively the aperture separation and the distance

Table 1. Mean and standard deviation of the calibrated particles distributions (units are μm).

Radius	100	139	200	240	378	504
Standard deviation	3.1	5.6	11	8.9	11.4	18.6

from the aperture plane to the object focal plane, see figure 3. M is the system nominal magnification at the object focal plane. Pereira and Gharib (2002) provide the detailed derivation of the functions F_x, F_y and F_z. Further analysis using 3D spatial correlation methods is performed to determine the three-dimensional velocity field.

Hence, the DDPIV technique is based on the matching of a pair of particle images in the case of a two-aperture system, or of a given pattern in a multiple-aperture system, for instance an equilateral triangle as in the three-aperture instrument used in our experiments. The principle thus differs from traditional triangulation methods in the fact that the matching is done in the image space and not in the object space. In addition, and in contrast with triangulation-based approaches, the optical axis is unique, implying a tremendous simplification of the optical configuration and of the calibration process, which is done once during the instrument assembly process.

6.2. Validation procedure

Our purpose in the following sections is to validate the methodology following the three steps:

(i) Determination of the volumetric distribution of the incident wavefront light intensity I_0 using calibrated particles.
(ii) Measurement of the light intensity scattered by different particle sets of known size distributions.
(iii) Comparison of the measured size distribution with the actual one, in terms of mean and deviation.

The calibrated particles are soda-lime glass micro-spheres and are NIST traceable. We consider six particle sizes, see table 1. The mean and standard deviation of each distribution are provided by the manufacturer.

In step (i), the volumetric distribution of $I_0(\mathbf{P})$ is calculated using equation (13), where the relative refractive index m_0 is equal to 1.128. The effective scattering angle θ depends upon the location $\mathbf{P}(X, Y, Z)$ of every calibration particle and is given by equation (11). In order to demonstrate that the incident light intensity I_0 is independent of the particle size a_0 used for its measurement, we calculate two distributions I_0^1 and I_0^2, respectively based on $a_0 = 240\,\mu$m and $a_0 = 378\,\mu$m.

Once I_0 is known, we proceed to step (ii), where different particle size distributions are measured. Table 2 lists the different cases, along with the I_0 calibration data used to process the scattering information.

Because these particles are not exactly mono-dispersed, and in addition to the measurement errors δ_{I_0} and δ_a, it is important to note that our validation procedure is expected to provide in step (iii) a total size deviation larger than the actual deviation.

In the following section, we describe the experimental setup. We underline the fact that the configuration used during the calibration phase should be exactly the same as in the size measurement phase. In practice, the calibration of a system like the DDPIV instrument can be made *in situ* immediately before the measurements, due to the self-contained nature of the instrument itself.

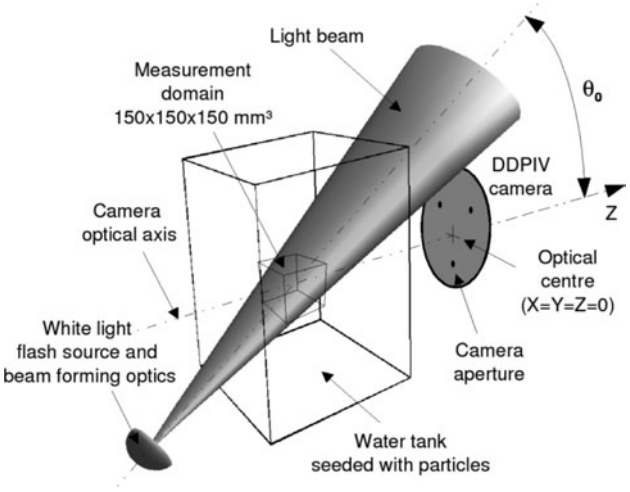

Figure 4. Experimental setup for the size measurement. $\theta_0 = 45^\circ$ is the illumination mean angle.

Table 2. Measurement matrix: I_0^1 is based on $a_0 = 240\,\mu$m and I_0^2 is based on $a_0 = 378\,\mu$m.

Particle actual mean radius a (μm)	I_0 distribution	
	1st case	2nd case
100	I_0^1	I_0^2
139	I_0^1	I_0^2
200	I_0^1	I_0^2
240	I_0^2	I_0^2
378	I_0^1	I_0^1
504	I_0^1	I_0^2

6.3. Experimental setup

The experimental setup is shown in figure 4. A water tank is filled with purified water, with no free surface to avoid the entrainment of air bubbles that would introduce a bias error into the measurement. The volume of measurement is illuminated by a broadband white light flash source in a forward scatter mode with a mean angle $\theta_0 = 45^\circ$. The beam formed by this light source and the optics is moderately divergent and allows the illumination of a volume of approximately $150 \times 150 \times 150\,\text{mm}^3$ in the centre of the tank. The volume is therefore fully mapped by the DDPIV camera used here. The light flashes are generated at the frequency of the camera (30 Hz), each pulse with an average duration of $10\,\mu$s. A different type of light source can be used, provided that the volume is fully illuminated. For instance, and with the additional optics necessary to expand the beam, a pulsed Nd:YAG laser could be used to map, simultaneously with the size measurement, the particle velocity field using techniques such as particle image velocimetry (PIV) or particle tracking velocimetry (PTV).

For the measurement of I_0^1 and I_0^2 and for each of the six cases listed in table 2, the water is seeded with the

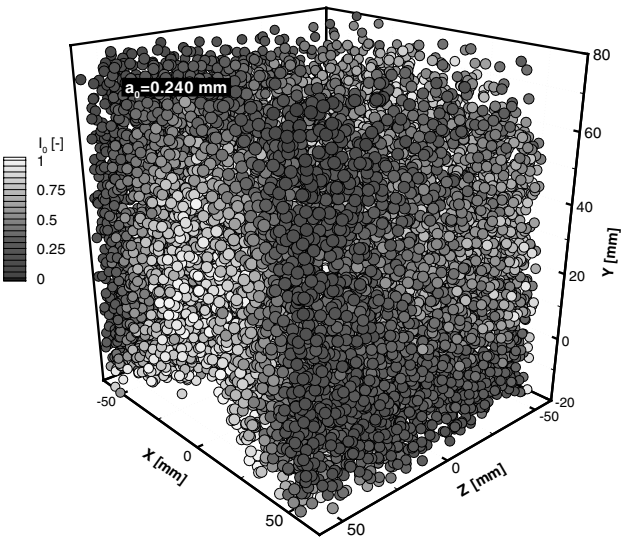

Figure 5. Spatial distribution of the incident intensity I_0^1: I_0^1 is normalized to unity; number of particles $\approx 35\,000$; measurement volume is shown translated to $Z = 0$ and size of particles is shown amplified for display.

corresponding particles and a stirring device is used to maintain them in continuous motion. The measurements are done with only one size of particles present in the tank at a time. Between two measurements, the tank is drained, cleaned and filled with new purified water before seeding with particles of a different size.

The DDPIV camera used in this experiment uses a special design described in Pereira *et al* (2000). The camera has one 8-bit CCD sensor, with a resolution of 1018×1008 pixels, assigned to each of the three apertures shown in figure 4. As per equation (9), the scattering is proportional to the square of the particle size and inversely proportional to the square of the distance from the particle to the camera optical centre. Thus, and because the *f*-number of the camera is constant by design ($\approx$25), the volume of interest is placed close to the camera to improve the light collection efficiency. The distance from the optical centre to the measurement volume is 600 mm. In addition, the dynamic range of the CCD sensors is adjusted internally through an electronic gain amplifier to a value where the intensity of the image formed by the largest particles is close, but never equal, to the saturation level. The setup thus optimized is kept unchanged during the different measurements listed in table 2.

6.4. Incident wavefront intensity

Figure 5 represents the measured three-dimensional particle field used to calculate the volumetric distribution of the incident light intensity I_0^1 (see table 2). The displayed volume size is $100 \times 100 \times 100$ mm^3. The dataset is obtained by adding up 200 instantaneous particle fields. Each particle is represented at its location $\mathbf{P}(X, Y, Z)$ and is greyed according to the value of its measured scattered intensity I_0^1. I_0^1 is shown in dimensionless form after normalization by a constant to avoid an unrealistic representation in W m^{-2} units of the actual intensity flux, as per equation (1).

Figure 6 shows the contours in the X–Y plane of the incident intensities I_0^1 and I_0^2, which have been averaged

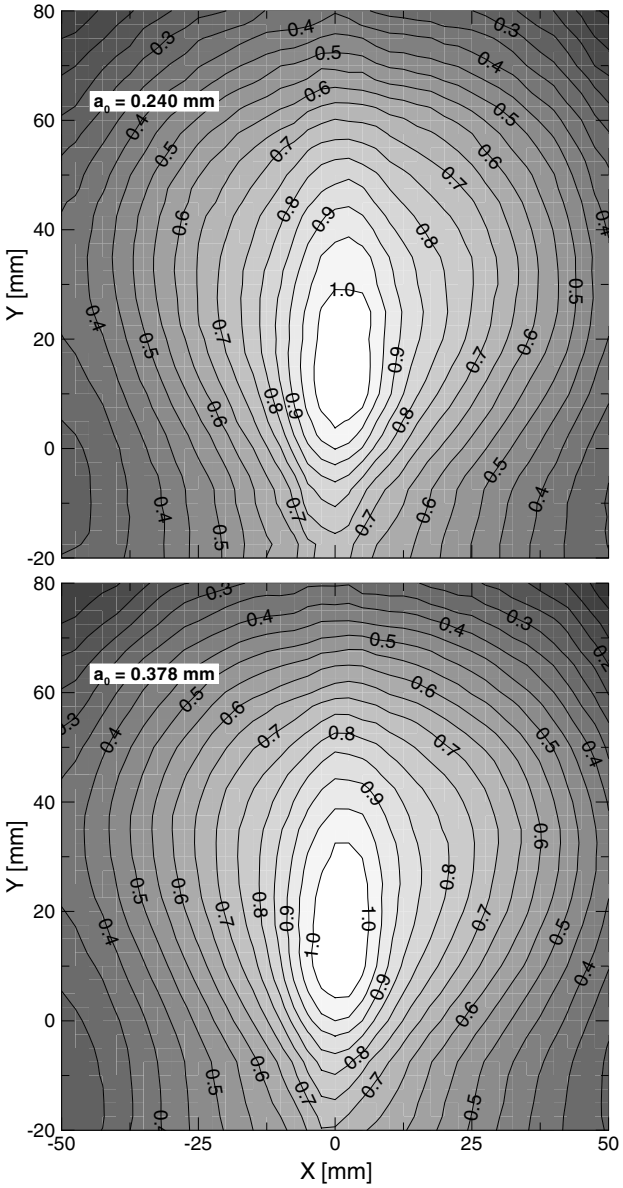

Figure 6. Z-averaged contours of the incident intensity: top, I_0^1; bottom, I_0^2.

along the Z-axis to provide a convenient basis for comparison between the two cases. Both are shown in dimensionless form as previously. A discrepancy lower than 1% is found between the two measurements, across the complete field. Most of this difference comes from the 50% lower particle density used for I_0^2, with respect to I_0^1. These results indicate that I_0 can be determined based on any calibrated particle size. They also show that a uniform incident light wavefront is not an absolute requirement, though it is recommended in order to get the same dynamic range across the entire observation domain.

6.5. Particle size

Following table 2, we perform the different experiments and determine the location and size distribution of each of the six size samples using the adequate and recently determined incident wavefront intensity I_0, as per equation (14). For $a = 240\,\mu$m and $a = 378\,\mu$m, which were used previously

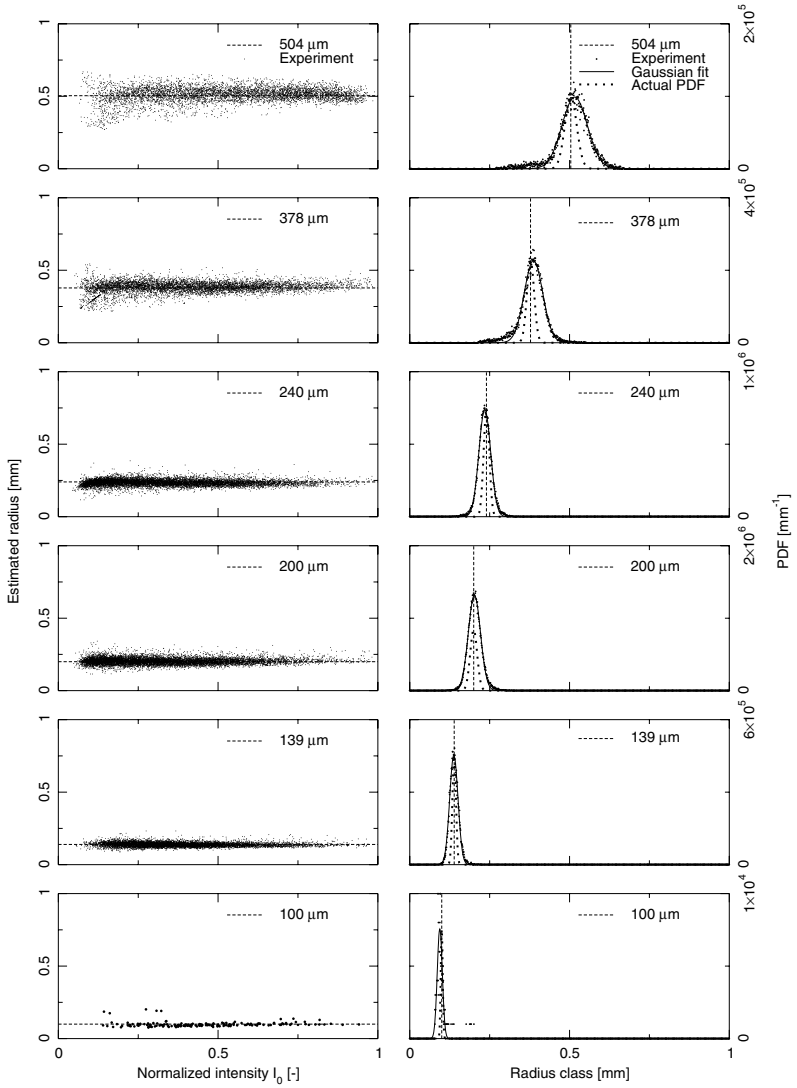

Figure 7. Left: estimated particle radius versus the incident wavefront intensity I_0 for the six size samples; right: experimental size probability density distributions and the corresponding Gaussian PDFs based on actual and measured values.

as calibration particles, new samples from the same batch are taken for the current measurements.

I_0^1 and I_0^2 are clouds of points randomly distributed inside the interrogation volume, see figure 5. Therefore, and for every scattering particle with intensity $I(a, \theta, \mathbf{P})$, it is necessary to define the incident intensity $I_0(\mathbf{P})$ at the particle location $\mathbf{P}$ from the neighbouring intensity points. If we consider a small sphere of radius r centred on $\mathbf{P}$, then we can write

$$I_0(\mathbf{P}) = \overline{I_0(\mathbf{P}_i)} \qquad \text{with} \quad \|\mathbf{PP}_i\| < r \tag{19}$$

where the values $I_0(\mathbf{P}_i)$ are taken either from the I_0^1 or from the I_0^2 experimental dataset, according to table 2. A sphere radius $r = 5$ mm is used here, which allows an average over a minimum of 10 neighbouring intensity points.

Figure 7 represents, on the left-hand side, the particle estimated radius a as a function of I_0, which is calculated following equation (19) and is represented in dimensionless form as before.

The normalized intensity I_0 spreads across the scale of intensities for I_0 is non-uniform across the volume, as illustrated in figures 5 and 6. Large particles located in low I_0 regions generate weak scattering, poor image contrast and thus increased errors both on the localization and on the intensity measurement of the particle image. This explains the larger spread for $a = 504\,\mu$m and $a = 378\,\mu$m found for $I_0 < 0.25$, that is essentially in the outermost regions, see the contour plots in figure 6.

On the right-hand side of figure 7, we represent the corresponding measured size density distributions, together with the Gaussian PDF curves based on the measured and actual values of the particle size mean and standard deviation. These are reported in table 3 and graphed in figure 8, where the error bars indicate the respective standard deviation.

As shown in figure 9 (top graph), the relative error on the mean radius is below 2%. The results obtained with I_0^2 are not significantly different from those obtained with I_0^1. Hence, the 1% discrepancy in intensity distribution has a minor impact on the mean value. In the same figure (bottom graph), we represent the corresponding standard deviations in terms of percentage of the reference radius. The measured standard deviation follows closely the trend of the actual standard deviation, except for $a = 100\,\mu$m due to the scarce

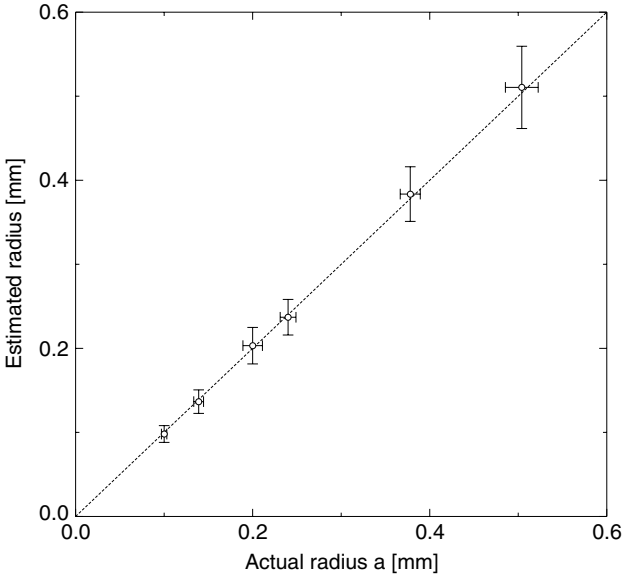

Figure 8. Estimated radius versus actual radius: measurements are based on I_0^1, except for $a = 240\,\mu$m (I_0^2); the dashed line is the unity slope line.

Table 3. Actual and measured mean and standard deviation.

	Radius mean (μm)					
Actual	100	139	200	240	378	504
Measured (I_0^1)	98.1	136.6	203.2	237	383.6	510.5
Measured (I_0^2)	97.7	136.5	203.4	237	383.6	511
	Radius standard deviation (μm)					
Radius:	100	139	200	240	378	504
Actual	3.05	5.55	11	8.9	11.35	18.55
Measured (I_0^1)	9.9	14	21.7	21.2	32.5	48.9
Measured (I_0^2)	9.5	12.8	19.9	21.2	32.5	44.5

experimental dataset. This indicates that the measurement error adds in quadrature with the actual particle size deviation, and represents 50–65% of the measured deviation.

One can trace back the measurement error using the error terms defined by equation (17). If we consider the first calibration case I_0^1, the calibration error δ_{I_0} is of the order of 7.8%. The subsequent deviation δ_a on the radius estimate is about 4.2%, which cumulates with the actual deviation value. The remaining error (1–2%) represents essentially the instrument errors, which derive from the optical aberrations, the mechanical misalignments and the processing algorithms. This error is also plotted in figure 9. The results obtained with I_0^2 show a reduced error because δ_a is lower in that case ($\approx$3.3%).

In other words, and considering the unique and three-dimensional nature of the measurement, our DDPIV instrument gives an accurate estimate of the mean size distribution, within 2% of the actual value. The measured error is two to three times larger than the actual error of the particle system. 40–50% of the measured error derives directly from the particle distribution used for the calibration, while 10–20% are instrument and processing errors.

To provide an indicative performance of the method with non-mono-disperse particle systems, we compose a mixture

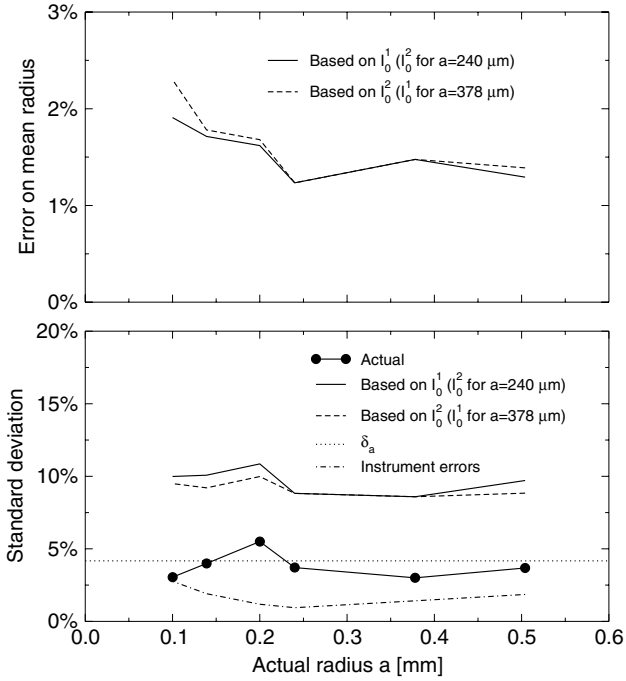

Figure 9. Top: error in the mean radius using I_0^1 and I_0^2; bottom: actual and measured standard deviations.

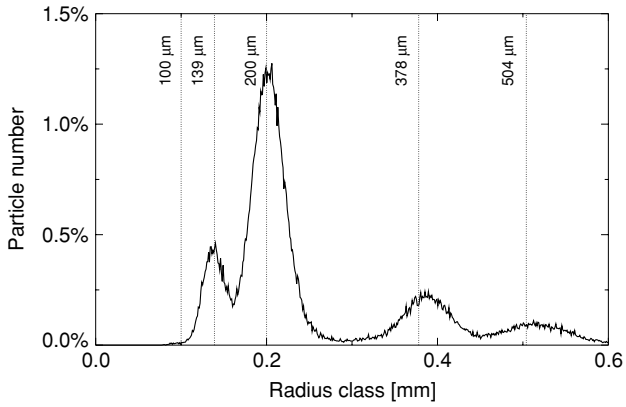

Figure 10. Size histogram for a mixture of five calibrated sizes; analysis performed with I_0^1.

of five particle types. Size $a = 240\,\mu$m is excluded in order to use the intensity dataset I_0^1. Figure 10 represents the measured size histogram of this mixture, where the particle number is normalized by the total population. The technique is found to perform correctly on well-separated size populations ($a = 139$, 378 and 504 μm). In the case of particles with close or overlapping size distributions, the respective histograms tend to merge, as clearly shown here for $a = 139\,\mu$m and $a = 200\,\mu$m. A calibration performed with truly mono-disperse particles would narrow the individual distributions and reduce their overlap.

7. Conclusion

A method has been devised for three-dimensional particle sizing of two-phase systems. The method is based on the determination of the volumetric distribution of the incident

light intensity inside the domain of interest. A ray-optics approximation of the Mie scattering theory for large spheres was used to derive the particle size from the measurement of their scattering intensity. An experimental procedure has been developed and tested with calibrated particles, using the DDPIV three-dimensional measurement technique.

The actual mean size is accurately estimated with less than 2% relative error. The measured standard deviation was found to be the sum of the actual standard deviation and of the technique measurement error, totalling an error 2–3 times larger than the actual value. The influences of the calibration and of the intensity flux variations were quantified. The calibration error was identified as being a major source of error, contributing as much as 50% to the final amount. Truly mono-disperse calibration particles are essential to minimize or cancel this error. Instrument and processing errors represent less than 20% of the overall error. The application of the method to a mixture of calibrated particles showed that the individual histograms were correctly identified, except when those were strongly overlapping.

Further assessment is desirable with a comparison against well-assessed (single) particle sizing techniques such as the phase-Doppler particle analysis. The combination of truly three-dimensional measurement with the levels of accuracy in sizing reported here provides a unique and easily implementable method that should help investigate cases of practical interest, especially bubbly flows.

Acknowledgments

The visit of Dr F Pereira to the California Institute of Technology was made possible by a fellowship of the *Fundação para a Ciência e a Tecnologia*, Portugal, under the supervision of Professor M V Heitor. The research was supported by the Office of Naval Research (contract N00014-97-1-0303), under the direction of Dr Ed P Rood and Dr Mark Hyman. The defocusing digital particle image velocimetry (DDPIV) technology is protected under a US patent filed by California Institute of Technology.

References

Bachalo W D 1994 Experimental methods in multiphase flows *Int. J. Multiph. Flow (Suppl.)* **20** 261–95

Billet M L 1985 Cavitation nuclei measurements—a review *Proc. Cavitation and Multiphase Flow Forum* (Albuquerque, NM: ASME) pp 31–8

Billet M L 1986 Cavitation nuclei measurements with an optical system *J. Fluids Eng.* **108** 366–72

Black D L, McQuay M Q and Bonin M 1996 Laser-based techniques for particle-size measurement: a review of sizing methods and their industrial applications *Prog. Energy Combust. Sci.* **22** 267–306

Bohren C F and Huffman D R 1983 *Absorption and Scattering of Light by Small Particles* (New York: Wiley)

Bongiovanni C, Chevaillier J P and Fabre J 1997 Sizing of bubbles by incoherent imaging: defocus bias *Exp. Fluids* **23** 209–16

Born M and Wolf E 1980 *Principles of Optics* 6th edn (Oxford: Pergamon)

Brena de la Rosa A, Sankar S V, Weber B J, Wang G and Bachalo W D 1989 A theoretical and experimental study of the characterization of bubbles using light scattering interferometry *Proc. Int. Symp. on Cavitation Inception (ASME)* vol FED-89 pp 63–72

d'Agostino L and Green S I 1992 Simultaneous cavitation susceptibility meter and holographic measurements of nuclei in liquids *J. Fluids Eng.* **114** 261–7

Damaschke N, Nobach H and Tropea C 2002 Optical limits of particle concentration for multi-dimensional particle sizing techniques in fluid mechanics *Exp. Fluids* **32** 143–52

Damaschke N, Rasmussen S, Tropea C and Woite A 2001 Global phase Doppler technique *Proc. 6th Int. Congress on Optical Particle Characterisation (Brighton, UK)*

Davis G E 1955 Scattering of light by an air bubble in water *J. Opt. Soc. Am.* **45** 572–81

Dean C E and Marston P L 1991 Critical angle light scattering from bubbles: an asymptotic series approximation *Appl. Opt.* **30** 4764–76

Glover A R, Skippon S M and Boyle R D 1995 Interferometric laser imaging for droplet sizing: a method for droplet-size measurement in sparse spray systems *Appl. Opt.* **34** 8409–21

Hawighorst A 1983 Drop size measurement in a vertical gas–liquid flow *Proc. Symp. Measuring Techniques in Gas–Liquid Two-Phase Flows (IUTAM, Nancy, France)*

Hofeldt D L and Hanson R K 1991 Instantaneous imaging of particle size and spatial distribution in two-phase flows *Appl. Opt.* **30** 4936–48

Katz J, Gowing S, O'Hern T and Acosta A 1983 A Comparative study between holographic and light-scattering techniques of microbubble detection *Proc. Symp. Measuring Techniques in Gas–Liquid Two-Phase Flows (IUTAM, Nancy, France)* pp 41–66

König G, Anders K and Frohn A 1986 A new light-scattering technique to measure the diameter of periodically generated moving droplets *J. Aerosol. Sci.* **17** 157–67

Maeda M, Kawaguchi T and Hishida K 2000 Novel interferometric measurement of size and velocity distributions of spherical particles in fluid flows *Meas. Sci. Technol.* **11** L13–8

Medwin H 1977 Acoustical determinations of bubble-size spectra *J. Acoust. Soc. Am.* **62** 1041–4

Mishima K and Hibiki T 1998 Development of high-frame-rate neutron radiography and quantitative measurement method for multiphase flow research *Nucl. Eng. Des.* **184** 183–201

O'Hern T J, d'Agostino L and Acosta A J 1988 Comparison of holographic and Coulter counter measurements of cavitation nuclei in the ocean *Proc. AIAA/ASME 1st National Fluid Dynamics Congress (Cincinnati, OH)*

O'Hern T J and Gore R A 1991 *Experimental Techniques in Multiphase Flows* vol FED-125 (ASME)

Pereira F and Gharib M 2002 Defocusing digital particle image velocimetry and the three-dimensional characterization of two-phase flows *Meas. Sci. Technol.* **13** 683–94

Pereira F, Gharib M, Dabiri D and Modarress D 2000 Defocusing digital particle image velocimetry: a 3-component 3-dimensional DPIV measurement technique. Application to bubbly flows *Exp. Fluids* **29** S78–84

Sheng Y Y and Irons G A 1991 A combined laser Doppler anemometry and electrical probe diagnostic for bubbly two-phase flow *Int. J. Multiph. Flow* **17** 585–98

Subbarao M and Surya G 1994 Depth from defocus: a spatial domain approach *Int. J. Comput. Vis.* **13** 271–94

Tassin A L and Nikitopoulos D E 1995 Non-intrusive measurements of bubble size and velocity *Exp. Fluids* **19** 121–32

Thompson B J 1974 Holographic particle sizing techniques *J. Phys. E: Sci. Instrum.* **7** 781–8

Ungut A, Grehan G and Gouesbet G 1981 Comparisons between geometrical optics and Lorenz–Mie theory *Appl. Opt.* **20** 2911–8

Vagle S and Farmer D M 1992 The measurement of bubble size distributions by acoustical backscatter *J. Atmos. Ocean. Technol.* **9** 630–44

Van de Hulst H C 1957 *Light Scattering by Small Particles* (New York: Wiley)

Zhu S, Pelton R H, Ajersch M, Towers M and Baird M H I 1993 Measurement of air bubble size using densitometer *Can. J. Chem. Eng.* **71** 269–77